Journal of Applied Polymer Science

Interfacial mechanical behavior of 3D printed ABS

Daniel P. Cole,[1] Jaret C. Riddick,[1] H. M. Iftekhar Jaim,[2] Kenneth E. Strawhecker,[3] Nicole E. Zander[3]
[1]U.S. Army Research Laboratory—Vehicle Technology Directorate, Aberdeen Proving Ground, Maryland 21005
[2]Materials Science and Engineering Department, University of Maryland, College Park, Maryland 20742
[3]U.S. Army Research Laboratory—Weapons and Materials Research Directorate, Aberdeen Proving Ground, Maryland 21005
Correspondence to: D. P. Cole (E-mail: daniel.p.cole.ctr@mail.mil)

ABSTRACT: We describe an experimental approach for characterizing the local mechanical behavior of acrylonitrile butadiene styrene (ABS) structures processed through fused deposition modeling. ABS test specimens processed in various build orientations were subject to multiscale mechanical tests as well as local morphology and chemical analyses. Instrumented indentation, local dynamic mechanical analysis, and atomic force microscopy tests were used to explore the mechanical behavior and morphology of build surfaces and weld interfaces. An interfacial stiffening effect was found for the majority of the specimens tested, with up to a 40% increase in the indentation elastic modulus measured with respect to the build surfaces. Raman spectroscopy mapping of the interfacial areas revealed ~30% less butadiene/styrene and butadiene/acrylonitrile ratios with respect to analysis of the build surfaces. The results provide insight into the multiscale behavior of additive manufactured structures and offer the potential to guide processing–structure–property understanding of these materials. © 2016 Wiley Periodicals, Inc. J. Appl. Polym. Sci. **2016**, *133*, 43671.

KEYWORDS: mechanical properties; properties and characterization; structure-property relations; viscosity and viscoelasticity

Received 23 February 2016; accepted 21 March 2016
DOI: 10.1002/app.43671

INTRODUCTION

Additive manufacturing (AM) technologies have several advantages over conventional manufacturing approaches, including lower design-to-fabrication times, complex geometry processing, lower part counts, and lower waste material.[1–3] The field of AM is quickly expanding and includes many promising applications, including progress in reconfigurable materials,[4] embedded electronics,[5] microsystem fabrication,[6] and tissue engineering.[7–10] Though advances in AM have enabled the rapid production of components with complex geometries, challenges with understanding the processing–structure–property relationships have limited more widespread use.

Fused deposition modeling (FDM) and other extrusion-based techniques (i.e., fused filament fabrication, melt extrusion manufacturing) are particularly popular AM methods for polymer processing. A typical melt extrusion process consists of a polymer feedstock material that is heated and forced through a print nozzle. The deposited material solidifies quickly, and is applied to the substrate layer-upon-layer allowing for the production of complex objects. However, since the nozzle velocity varies throughout the printing process, the amount of the melted feedstock as well as the melt temperature, surface energy, and viscosity may also vary with respect to the feed rate.[11]

The kinetics of the melt extrusion printing process are important for understanding the processing–structure–property relationships in these extrusion-based methods.[12] During AM processing, forces acting on the material within the nozzle are relieved once the material exits the nozzle, allowing elastic energy within the melt to be released and causing radial expansion. The bond strength will be controlled in part by the temperature history of the bead–bead interface.[13] The final structure of the 3D printed component is a function of the thermal properties of the material (i.e., thermal conductivity, heat capacity, etc.), the thermal history of the materials, and the printing conditions. Attempts have been made to model the bonding between adjacent beads, which occurs through viscous flow and molecular diffusion processes.[14,15] For two adjacent cylindrical beads of diameter $2r$, a neck length $2z$ can be used to characterize the bond figure of merit (see Figure 1). A model based on Newtonian sintering was used to predict the neck length growth using a dimensionless parameter $\omega = \sin^{-1}(z/r)$ with respect to time t:

$$\frac{d\omega}{dt} = 2^{-\frac{5}{3}} \cdot \frac{\rho}{r_o n} \cdot \frac{\cos\omega \cdot \sin\omega \cdot (1-\cos\omega)^{1/3}}{(1-\cos\omega) \cdot (1+\cos\omega)^{1/3}} \quad (1)$$

where r_o is the initial filament radius, ρ is the surface tension, and n is the viscosity.[14,15] Among other assumptions, eq. (1) is

Additional Supporting Information may be found in the online version of this article.

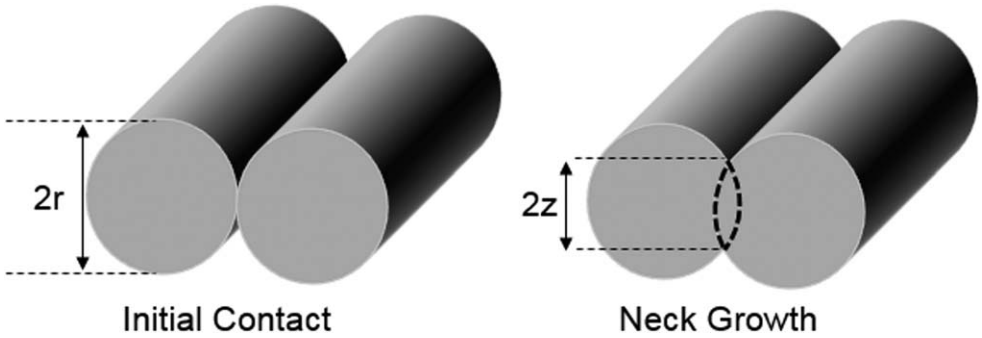

Figure 1. Schematic of initial deposition of adjacent beads (left) and then neck growth across bead-bead interface (right).

limited to describing a process at constant temperature and viscosity, whereas these parameters will typically vary throughout the FDM process.

Common FDM feedstock materials include polyetherimide, polycarbonate, polyphenylsulfone, and acrylonitrile butadiene styrene (ABS).[11] ABS is a particularly popular choice and is composed of three monomers: acrylonitrile, butadiene, and styrene.[16,17] The toughness of the amorphous, glassy styrene acrylonitrile monophase is increased by the addition of the non-continuous rubbery butadiene phase. Several parameters control this morphology-toughness behavior, including particle size, particle nearest neighbor distance, matrix particle adhesion strengths, and the mechanical properties of particles themselves.[18] While the ratios of the three constituents may be varied for a given application, the resulting polymer is typically formulated to achieve a balance of toughness, strength, and temperature resistance. Typical ABS blends consist of small butadiene particles with an average size of 200 nm; however, there is reportedly a large size distribution, with particles as large as 50 μm typically present.[19]

Previous mechanical characterization tests of 3D printed polymer structures have been mostly limited to the macroscale. Several groups have reported bulk mechanical anisotropy in 3D printed components that was linked to raster orientation.[20,21] Build orientation was found to cause alignment of the polymer molecules along the axis of deposition, while volumetric shrinkage in the printed beads resulted in weak interlayer interaction and high porosity.[20] Bulk mechanical testing and subsequent Raman spectroscopy measurements of ABS specimen fracture surfaces have revealed defects originating from the relatively large butadiene particles.[19] Flores *et al.* looked at microhardness studies of several thermoplastics and found correlations to bulk mechanical behavior such as elastic modulus and yield strength, although these tests were limited to compression molded materials.[22]

For AM-processed materials, where properties are variable with respect to spatial location and a high density of microstructural heterogeneities exist, local mechanical techniques are needed to fully understand processing–structure–property relationships. Instrumented indentation, commonly referred to as "nanoindentation" (NI), is a popular technique for probing local mechanical properties of a sample.[23] During indentation, the force and displacement are continuously monitored with nanoNewton and nanometer resolution, respectively, making the technique attractive for applications in which small volumes of materials need to be examined. Standard NI theory assumes specimens are flat, isotropic half-spaces, although tests on substrate-film systems,[24,25] composite materials,[26,27] samples with edges,[28,29] and graded materials[30–32] have been demonstrated with appropriate modifications. Indentation studies accounting for viscoelastic behavior of materials have also been demonstrated; a particularly challenging issue for applying depth-sensing indentation to a material with time-dependent mechanical behavior is creep, which can complicate the assumed linear elastic response during the initial stages of unloading.[33–36]

In the present work, we introduce a method for characterizing the local properties of ABS specimens processed through FDM. The bulk mechanical behavior of FDM tensile specimens processed with various build orientations is explained through NI, local dynamic mechanical analysis, atomic force microscopy (AFM), and Raman spectroscopy. In addition, an advanced NI analysis is included in the Supporting Information that accounts for the non-standard geometry of the printed components.

Background: Nanoindentation Theory

The standard Oliver–Pharr indentation method uses load P versus displacement h data and a calibrated tip area function $A(h)$ to determine the elastic modulus E and hardness H of a material.[23] H is determined at the maximum load P_{max} according to:

$$H_{OP} = \frac{P_{max}}{A} \tag{2}$$

Here, A is calculated from the contact depth h_c, which accounts for the deformation that occurs in the surrounding material not directly in contact with the indenter:

$$h_c = h_{max} - \epsilon \cdot \frac{P_{max}}{S} \tag{3}$$

ϵ is a tip geometric constant approximately equal to a value of 1 for flat punch and spheroconical tips, 0.72 for a conical tip, and 0.75 for a Berkovich tip.[23] S is the stiffness of the tip-sample contact and is defined by the slope of the unloading curve at h_{max}:

$$S = \frac{dP}{dh} \tag{4}$$

S is used to determine a reduced elastic modulus of the tip-sample contact through,

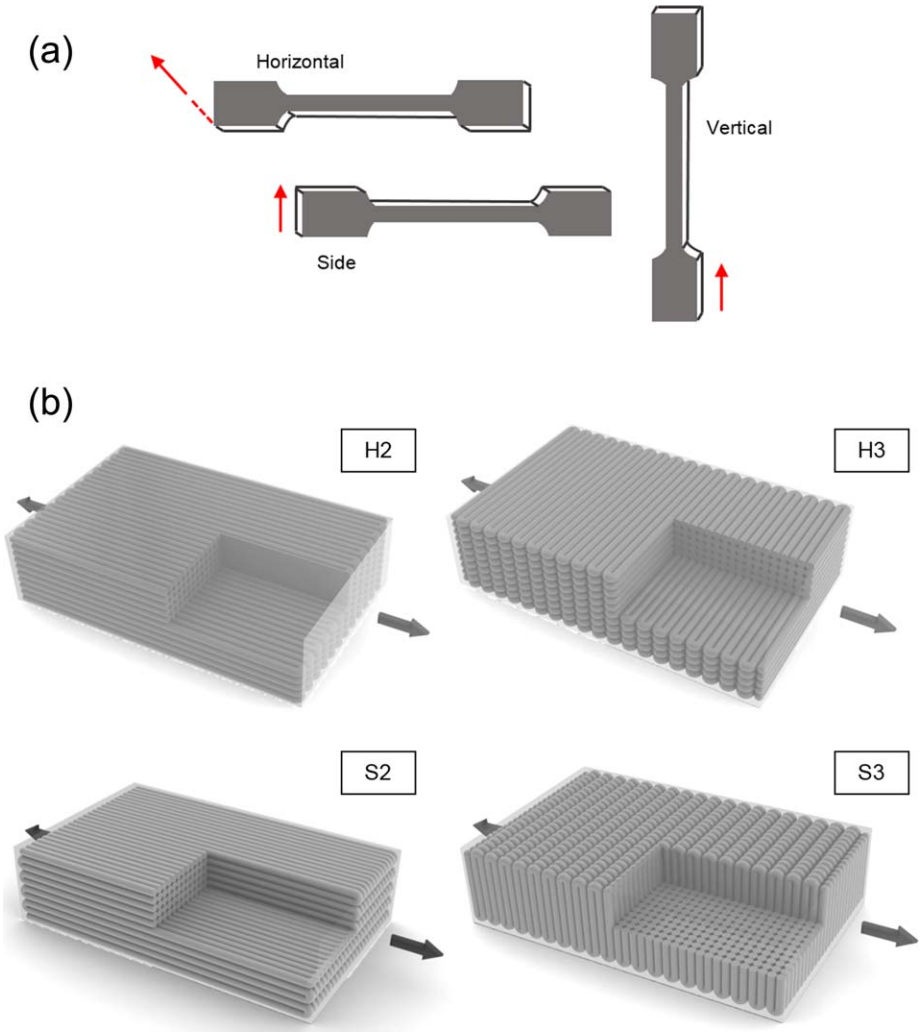

Figure 2. (a) Schematic of various dogbone build directions used in this study. Arrow indicates direction of subsequent layer deposition. (b) Examples of various build directions and raster orientations of dogbone specimens targeted for local mechanical characterization. Arrows indicate tensile loading direction and is defined as the 0° raster orientation. H2 = Horizontal 0°, H3 = Horizatonal 90°, S2 = Side 0°, S3 = 90°. Note that the H2/S2 configurations result in the longest rasters, while the H3/S3 configurations result in relatively short rasters. [Color figure can be viewed in the online issue, which is available at wileyonlinelibrary.com.]

$$E_r = \frac{S}{2\beta} \cdot \sqrt{\frac{\pi}{A(h_c)}} \tag{5}$$

where β is an additional constant related to the indenter geometry (a value of ~1 for spheroconcial geometry). The elastic modulus of the sample can then be found through the following relationship which accounts for the deformation of both the tip and sample during indentation:

$$\frac{1}{E_r} = \frac{1-\nu_i^2}{E_i} + \frac{1-\nu_s^2}{E_s} \tag{6}$$

where E_i, E_s, ν_i and ν_s are the elastic modulus and Poisson's ratio of the indenter and sample, respectively. The quasi-static analysis outlined above does not consider viscoelastic effects, which are often seen in testing of polymeric materials.[33–36] During indentation, the S used in eq. (5) is only valid for a specimen that undergoes pure elastic recovery during the initial stage of unloading. To account for anelastic effects during quasi-static indentation tests, Feng *et al.* included a correction due to creep:

$$\frac{1}{S} = \frac{1}{S_a} + \frac{\dot{h}_h}{|\dot{P}|} \tag{7}$$

where S_a is the apparent stiffness measured during unloading, $\dot{h}_h$ is the probe velocity at the end of the load hold, and $|\dot{P}|$ is the unload rate.[36] Creep effects in indentation tests can be mitigated by (1) increasing hold times before unloading and (2) increasing loading/unloading rates.[36] Further local viscoelastic behavior can be characterized through dynamic nanoindentation studies.[34,35] For time dependent indentation studies, a loss modulus E_r can be defined as

$$E_r = \frac{\omega C_s}{2\beta} \cdot \sqrt{\frac{\pi}{A(h_c)}} \tag{8}$$

where ω is the angular frequency and C_s is the damping of the system.

The standard indentation theory described above assumes the sample is a flat, semi-infinite half space. Modifications to the

Table I. Summary of Printed Samples Used in This Study

Designation	Build direction	Raster orientation
H1	Horizontal	(+/− 45°)
H2	Horizontal	(0°)
H3	Horizontal	(90°)
H4	Horizontal	(0°–90°)
S1	Side	(+/− 45°)
S2	Side	(0°)
S3	Side	(90°)
S4	Side	(0°–90°)
V1	Vertical	(+/− 45°)
V2	Vertical	(0°)
V3	Vertical	(90°)
V4	Vertical	(0°–90°)

Raster orientation is the angle between the print direction and loading direction during bulk tensile testing (i.e., long axis of dogbone specimen)

theory must be made if the samples violate these assumptions.[37,38] Recent work on the indentation of cylindrical fibers includes modified analyses that account for sample geometry.[39,40] The Supporting Information includes an analysis for determining a modified contact depth h_c^* for sample curvature. For the current work, these modifications were initially considered due to the cylindrical geometry of the printed beads.

EXPERIMENTAL

Specimen Processing

Specimens were processed using ABS-M30 natural feedstock via an FDM system (Stratasys Fortus 400mc). Tensile specimens were processed according to ASTM D638-03. During processing, the feedstock filament was heated to ~95°C. A T10 tip size was used, resulting in molten filament with a width of ~200 μm. Specimens were printed in three different build orientations: (1) horizontal (H), built layer-by-layer up the dogbone short axis, (2) side (S), printed up the medium length axis, and (3) vertical (V), built up the dogbone long axis [see Figure 2(a)]. For every build orientation, four separate raster angles were utilized: (a) 0° with respect to the tensile specimen long axis (parallel with the loading path), (b) 90°(perpendicular with the loading path), (c) alternating layers of +45° and −45° (with respect to the loading direction), and (d) alternating layers of 0° and 90°. Figure 2(b) shows example renderings of the samples targeted for local mechanical characterization, while Table I summarizes the entire set of build designs used in this study.

Optical Microscopy

Optical measurements of the printed surfaces were performed using a laser scanning microscope (LSM 700, Zeiss) with a 405 nm laser. Tests were run in fluorescence mode. 3D profiles were obtained by taking multiple optical slices through the z-stack function. Raw data were exported to ConfoMap (Digital Surf) for analysis; images were flattened using a plane level and pinholes in the measured data were filled using the "fill hole" function.

Bulk Mechanical Testing

Bulk tensile testing of printed dogbone test specimens were run according to ASTM D638-03 using an Instron 5565 Tensile Tester with a 5 kN load cell and biaxial strain gages (Micro-Measurements CEA-06-125UT-350). The test setup was first calibrated using an aluminum standard. Tests were performed at 1.3 mm min^{-1}, while axial and transverse strains were continuously recorded (StrainSmart System, Vishay Precision Group).

Nanoindentation

Instrumented indentation tests were performed using a Hysitron TI-950 TriboIndenter with a 350 nm diamond conical tip (60° included angle). Samples were approached using a 2 μN setpoint. Samples were imaged, repositioned, and their 3D shape was determined using the scanning probe feature of the TriboIndenter. Indentation tests were executed in force control, with a maximum applied force of 1000 μN which led to contact depths ranging from 1.0 to 1.5 μm. A drift correction was performed prior to indentation using a preload of 1 μN for 20 s. A trapezoidal load profile was used, with a quasi-static rate of 125 μN s^{-1} and a 4 s hold immediately following the load segment to permit relaxation of the material prior to unloading. In order to measure sample elastic properties, E_i and ν_i were taken to be 1140 GPa and 0.07,[23] respectively, and ν_s was measured at 0.365 via global mechanical experiments according to ASTM D638-03 (ratio of transverse and axial strains up to the proportional limit). The characteristic unloading "nose" seen at times for viscoelastic materials was not observed; however, a correction to the stiffness measurement was made using eq. (7) in order to account for any creep effects.

For every build, a minimum of four local regions were targeted: two on the printed build surface and two within the build–build interfacial areas (see Figure 3). For every targeted region, a minimum of five local measurements were executed, with every indent performed a minimum of 5 μm from previous tests. Indentations were restricted to the 0° and 90° builds within the side and horizontal samples since these designs contained the processing parameter extremes. The relative poor quality of the vertical builds resulted in a surface roughness typically too high

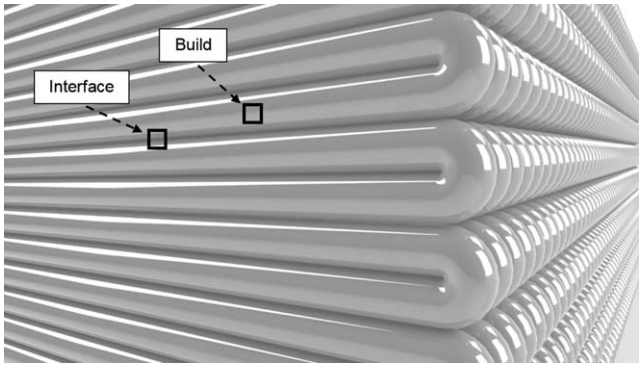

Figure 3. Schematic showing closeup of printed component. Highlighted areas indicate indentation areas targeted on the printed build surface as well as indentation areas targeted in interfacial regions.

Table II. Summary of Bulk and Local Mechanical Properties for ABS Test Specimens

Sample	$E_{tensile}$ (GPa)	σ_t (MPa)	$\sigma_t/\sigma_{t0°}$	E_{build} (GPa)	E_{int} (GPa)	H_{build} (MPa)	H_{int} (MPa)
H1 (+/− 45°)	2.42 ± 0.10	27.8 ± 0.9	0.85	-	-	-	-
H2 (0°)	2.69 ± 0.01	32.6 ± 1.1	1.00	2.09 ± 0.10	2.34 ± 0.13	253.9 + 6.6	253.8 + 8.4
H3 (90°)	2.45 ± 0.07	15.3 ± 0.9	0.47	1.97 ± 0.04	2.32 ± 0.09	262.1 + 5.3	272.2 + 28.9
H4 (0°-90°)	2.59 ± 0.05	25.7 ± 1.8	0.79	-	-	-	-
S1 (+/− 45°)	2.66 ± 0.03	29.6 + 2.0	0.87	-	-	-	-
S2 (0°)	2.79 ± 0.05	34.2 ± 1.5	1.00	2.05 ± 0.03	2.99 ± 0.37	256.2 ± 6.8	269.7 ± 12.0
S3 (90°)	2.53 ± 0.04	24.2 ± 0.7	0.71	2.05 ± 0.17	1.73 ± 0.05	257.0 ± 11.5	264.3 ± 10.9
S4 (0°-90°)	2.65 ± 0.04	29.1 ± 0.2	0.85	-	-	-	-
V1 (+/− 45°)	2.76 ± 0.03	19.8 ± 2.2	1.31	-	-	-	-
V2 (0°)	2.77 ± 0.13	15.1 ± 2.0	1.00	-	-	-	-
V3 (90°)	2.67 ± 0.05	12.4 ± 5.4	0.82	-	-	-	-
V4 (0°-90°)	2.74 ± 0.11	13.6 ± 1.1	0.90	-	-	-	-

for repeatable local measurements and were thus excluded from indentation tests.

Local Dynamic Mechanical Analysis via Indentation

Local dynamic mechanical analysis (DMA) studies were performed on bead–bead interfacial regions using the Hysitron TI-950 Triboindenter and a 350 nm conical diamond probe. The same quasi-static loading profile was implemented with a 1000 μN force initially applied, followed by a 4 μN dynamic load over a frequency range of 0.1–100 Hz. The dynamic load resulted in a dynamic amplitude of ~1 nm. The storage E' and loss E'' modulus were recorded according to eqs. (5) and (8), respectively.

Scanning Probe Microscopy

Scanning probe measurements were performed using an Asylum Research Cypher atomic force microscope (AFM). The AFM tips used were Si cantilevers coated in Al, with typical radius of curvature, natural frequency, and stiffness of 10 nm, 120 kHz, and 10 N/m, respectively (AC200TS). Topography and phase mapping were performed in alternating contact mode with scanning rates of ~1 Hz. For local modulus mapping, a spin-cast 2.7 GPa polystyrene film reference sample was used to calibrate the tip area function.

Raman Spectroscopy

Chemical analyses of ABS builds and bead–bead interfaces were performed using a Raman Spectroscopy microscope (LabRAM, JY Horiba) with a 532 nm laser. A calibration of the instrument was performed on a Si wafer prior to testing. A spot size less than 1 μm^2 was used which ensured sufficient resolution to target areas on and between the printed beads. Both area mapping and line scans were performed on bead surfaces and bead–bead interfacial areas for the H2, H3, S2, and S3 samples. Data were recorded ~1.5 μm apart in both x and y directions and the Duoscan mode feature was used to average the signal from adjacent data. Therefore, each reported signal is the average of three scans. Data were analyzed using the Labspec 5 software for baseline corrections and for plotting the ratio of the integrated areas under the Raman peaks.

X-ray Photoelectron Spectroscopy

Surface compositional analysis was performed using a Kratos Axis Ultra 165 X-ray photoelectron spectroscopy (XPS) system equipped with a hemispherical analyzer. Sampling areas of 27 μm and 55 μm diameter in 40 μm steps across the sample were irradiated with a 140 W monochromatic Al Kα (1486.7 eV) beam and a take-off angle of 90°. The XPS chamber pressure

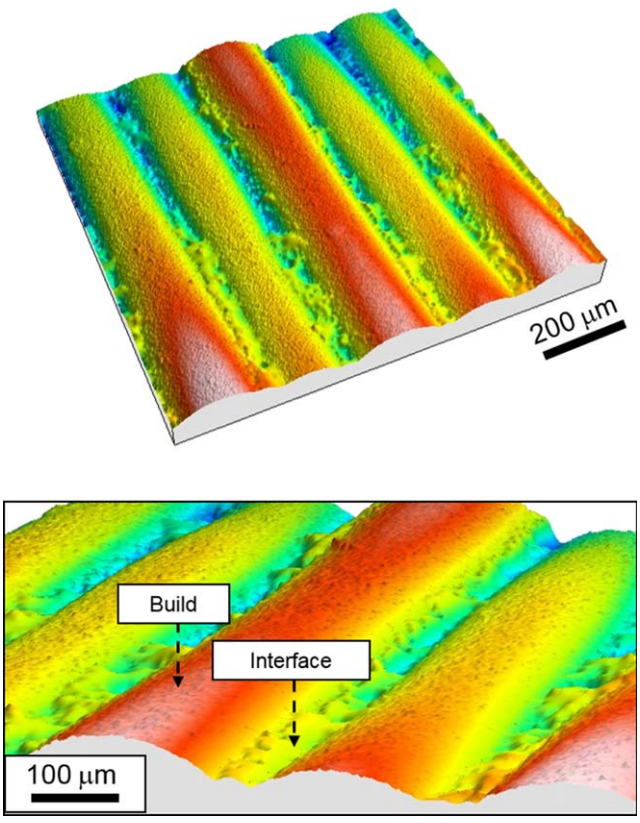

Figure 4. Laser scanning microscope images of a 3D printed specimen taken in fluorescence mode. Regions targeted for tests on bead surface and interfacial regions are denoted. [Color figure can be viewed in the online issue, which is available at wileyonlinelibrary.com.]

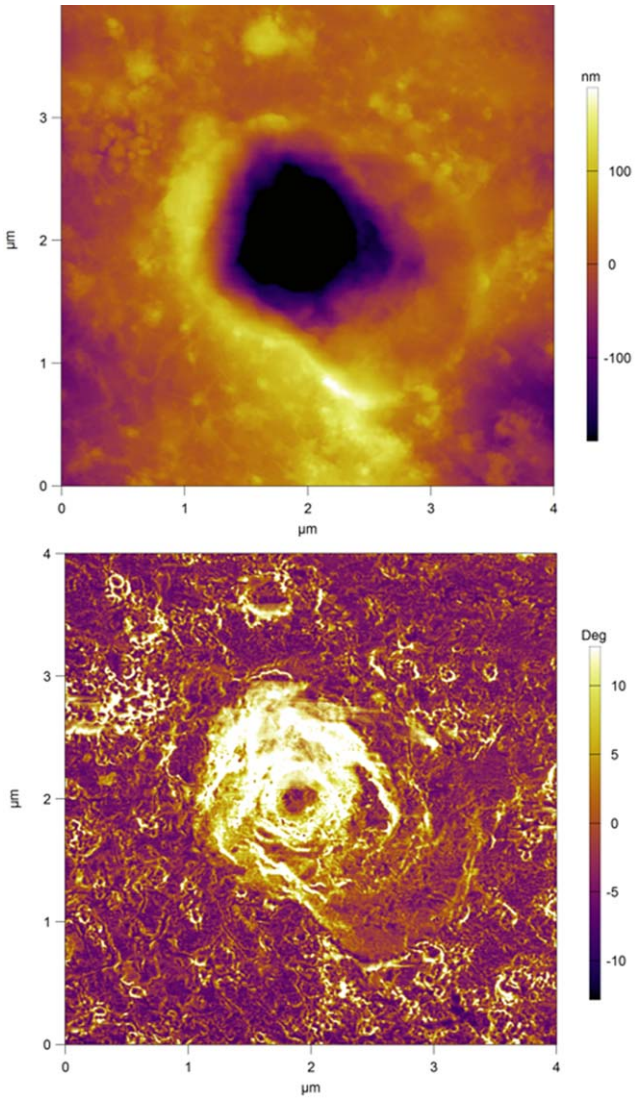

Figure 5. 4 μm height (Top) and phase (Bottom) atomic force microscopy (AFM) images of residual impression in 3D printed ABS via instrumented indentation. [Color figure can be viewed in the online issue, which is available at wileyonlinelibrary.com.]

was maintained between 10^{-9} - 10^{-10} Torr. Elemental high resolution scans were conducted with a 20 eV pass energy for the C 1s and N 1s core levels. A value of 284.6 eV for the hydrocarbon C 1s core level was used as the calibration energy for the binding energy scale. Data were processed using Casa XPS software. All reported atomic percentages are the average of $n = 2$ measurements on a minimum of three replicate samples.

RESULTS AND DISCUSSION

Table II includes a summary of the bulk mechanical tests of the tensile specimens characterized using ASTM standard D638-03. The tensile elastic modulus E_t was fairly consistent across the various builds, with the samples printed with the 0° raster orientation (parallel with tensile loading axis) demonstrating a slightly higher elastic response. The effect of the printing orientation was much more pronounced for the specimen tensile strength σ_t. Both the build direction and raster orientation parameters had a significant effect on σ_t, with the 0° raster showing strengths typically much higher than the other rasters. A $\sigma_t/\sigma_{t0°}$ parameter was defined which compares the tensile strengths of the particular build with the 0° raster. For the horizontal builds, $\sigma_t/\sigma_{t0°}$ was as low as 0.47, while $\sigma_t/\sigma_{t0°}$ for the side builds reached a minimum of 0.71. The vertical builds were the exception, with the +/−45° samples demonstrating the highest relative σ_t. However, all vertical build samples showed a relatively low σ_t, so it is difficult to draw conclusions about this particular set of results.

As expected, the global mechanical performance was improved through a higher degree of orientation between the printed builds and the loading direction. What was less clear was how the mechanical properties for a particular raster orientation might vary depending on slight differences in neighboring bead interactions. To examine this behavior, nanoindentation experiments were performed on and between printed beads. Figure 4 shows a 3D laser scanning microscope image of a sample surface that includes several printed beads and interfacial regions. Figure 4 also displays a zoomed view of the sample surface and

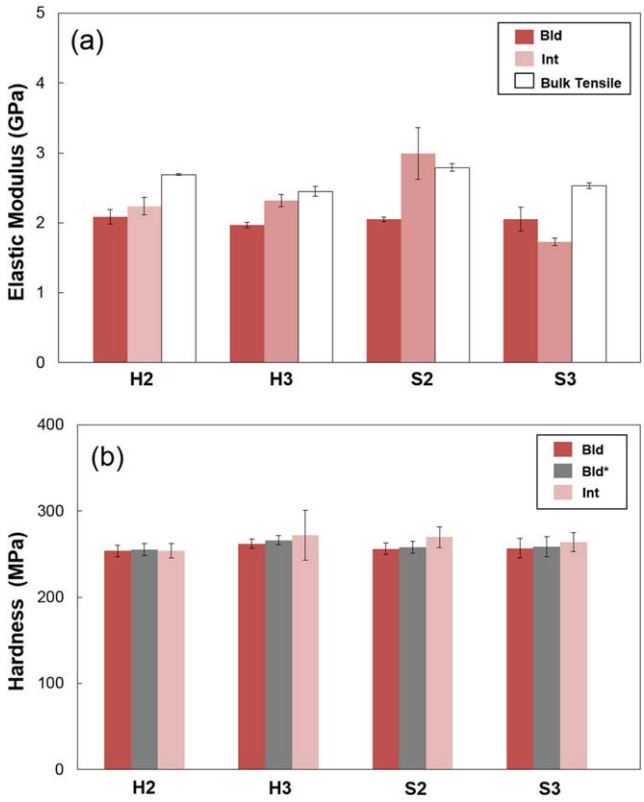

Figure 6. (a) Elastic modulus and (b) Hardness results for local mechanical tests on printed build surfaces (Bld) and interfacial regions (Int). Bulk tensile data included in (a) for comparison to local mechanical behavior. Bld* values in (b) represent the values determined through a modified indentation analysis that accounts for an area function correction due to sample curvature. [Color figure can be viewed in the online issue, which is available at wileyonlinelibrary.com.]

denotes typical areas of interest targeted for indentation tests. Indentation tests were performed on relatively smooth areas that were located through a series of optical inspections and scanning probe measurements, followed by slight sample-tip repositioning. Figure 5 displays AFM height and phase images of a typical indent. The residual spheroconical impression can be seen with a limited amount of pile-up; therefore, corrections in the tip area function for pile-up were not considered. However, a correction for creep effects on the indentation response was included by calculating the average probe velocity over the final 0.5 s of the hold segment. Equation (7) was used to calculate an updated stiffness that included creep contributions to the unloading segment. We note that the characteristic unloading "nose" often seen in indentation of some polymeric materials was not apparent, yet the contribution due to creep still had a meaningful effect on the measured stiffness. An additional correction considered for quasi-static tests was an area function modification due to tests on the curved build surfaces. For the build parameters and testing conditions used in the current study, the area function modification was negligible. However, the correction will become more relevant for particular processing/testing parameters, particularly for decreasing build diameters and increasing tip radii. More information on area function modifications can be found in the Supporting Information.

Table II includes a summary of the local mechanical tests; Figure 6 shows a graphical representation of the data. Tests on the surface of the printed builds are denoted E_{build} and H_{build} for indentation elastic modulus and hardness, respectively. Tests on the interfacial areas between the printed builds are denoted E_{Int} and H_{Int}. In general, the indentation elastic modulus values agreed reasonably well with the elastic modulus values found through bulk mechanical testing. The local results were typically 20–30% lower than the bulk results, which is most likely due to fundamental differences in the testing methods (indentation vs. tensile).

The more interesting quasi-static indentation result was the variation in the local mechanical properties at different locations within a given sample. Indentations on the interfacial regions typically showed a stiffer response than tests on the corresponding printed build surfaces. The local elastic modulus measurements comparing the interfaces and respective builds were all statistically significant ($P < 0.05$). The most pronounced example of this behavior was seen in the S2 samples, where E_{Int} was on average 40% higher than the E_{build}. The S2 sample was the side-printed design processed using a 0° raster orientation (along long dogbone axis), and thus one of the configurations with the shortest average time allowed for bead–bead melt interaction. Alternatively, the S3 build, the side-printed design with the 90° raster orientation, showed the opposite effect. In this case, E_{Int} was ~15% lower than E_{build}, which is attributed to the relatively long average time allowed for neighboring beads to interact.

Compared to the local elastic modulus tests, the local hardness measurements were less sensitive to interfacial and build areas [see Figure 6(b)]. In fact, comparisons between H_{build} and H_{Int} for the S2, S3, H2, and H3 samples were not statistically significant (95% confidence interval). Figure 6(b) also includes hardness results determined through an indentation analysis that accounts for the over-estimation of the tip-sample contact area due to the curvature of the printed builds (see Supporting Information for further details). For the given set of test parameters (i.e., R, r, θ, h_c), H^* was typically within 1% of the hardness found through the standard indentation theory, and a similar result was found for the elastic modulus measurements. However, the area function analysis would become more important as the build radius decreases, tip radius of curvature increases, and/or the tip half angle increases.

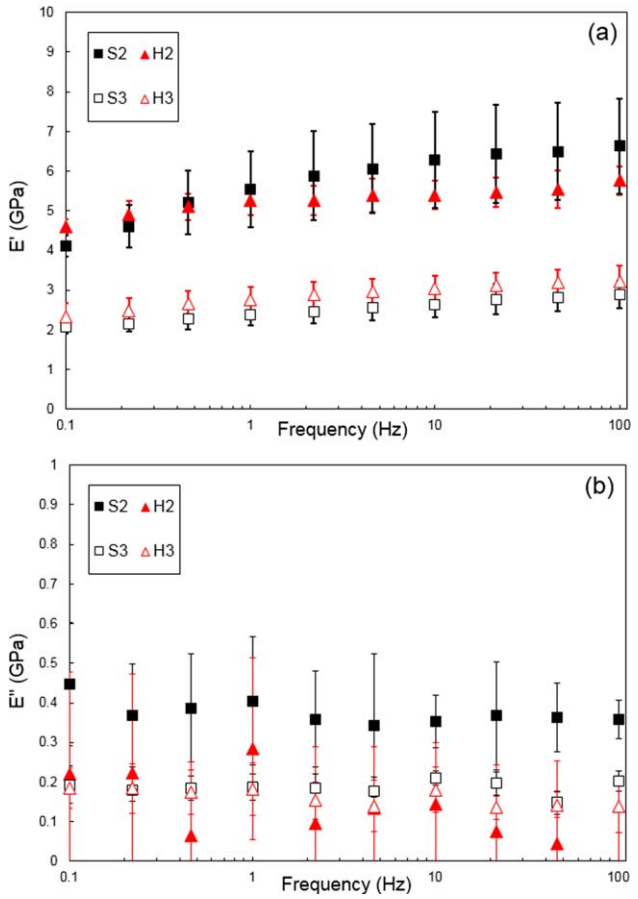

Figure 7. Local dynamic mechanical analysis (DMA) tests on S2, S3, H2, and H3 interfacial regions. (a) Storage modulus and (b) loss modulus data over a frequency range of 0.1–100 Hz. [Color figure can be viewed in the online issue, which is available at wileyonlinelibrary.com.]

The mechanical behavior of the interfacial areas was further examined using local DMA. The same loading profile used for the quasi-static tests was initially used for the DMA tests in order to sample a similar volume of material at the interface. On top of the quasi-static test, dynamic measurements were made over a frequency range of 0.1–100 Hz. Figure 7 shows E′ and E″ results from the local DMA tests on the S2, S3, H2, and H3 interfaces. The storage moduli for the S2 and H2 interfaces were typically higher than the storage moduli for the S3 and H3 interfaces. The S2 interface was typically the stiffest interface and S3 the most compliant interface over the tested frequency

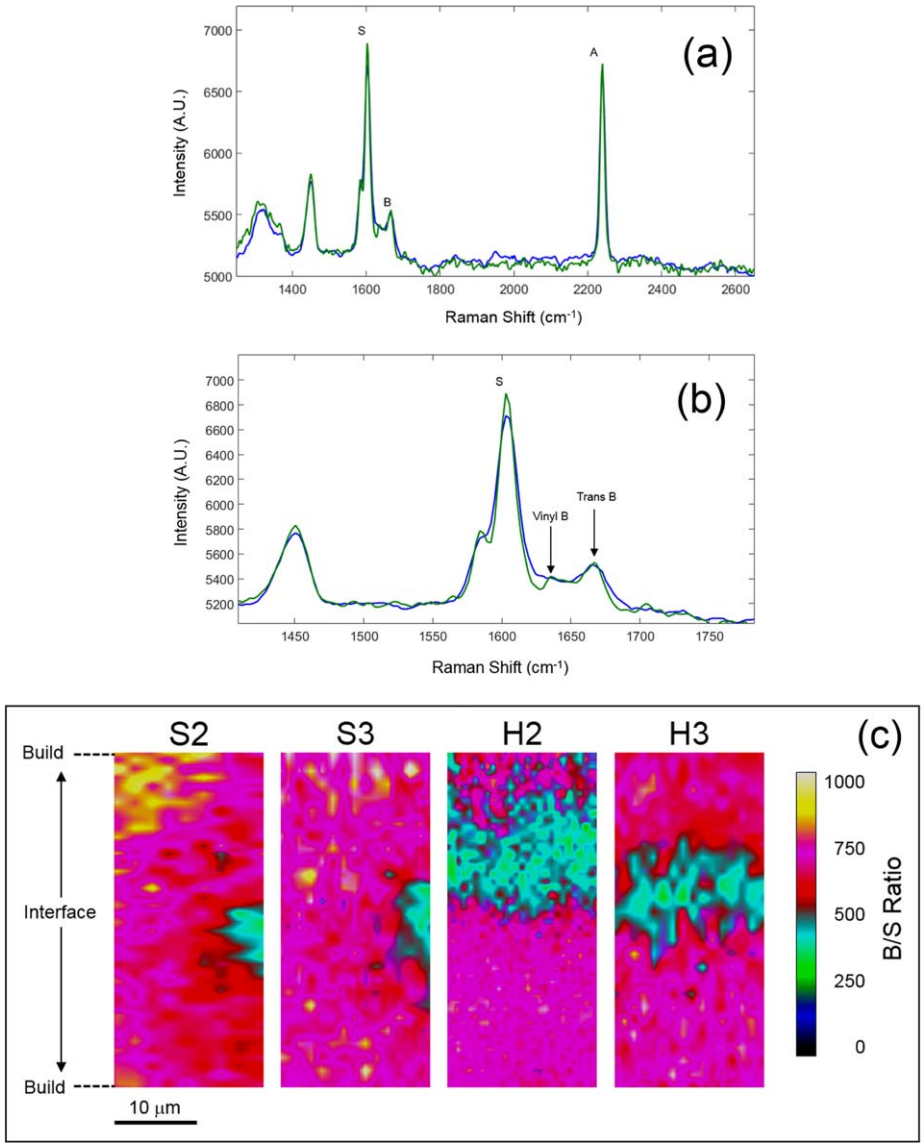

Figure 8. (a) Raman spectra shown for multiple scans on S2 specimen. (b) Zoomed in spectra for scans shown in (a). (c) Raman spectroscopy maps of the S2 (side 0°), S3 (side 90°), H2 (horizontal 0°), and H3 (horizontal 90°). Scale bar indicates relative B/S ratio in arbitrary units. [Color figure can be viewed in the online issue, which is available at wileyonlinelibrary.com.]

range. This result was fairly consistent with the quasi-static interfacial tests that showed a stiffer interfacial response for the samples built with long rasters and thus shorter average times for bead–bead interactions in the melt state. Differences in the loss modulus for the various builds were less clear, with the majority of the tests overlapping.

To help interpret the local mechanical behavior, Raman spectroscopy mapping was performed on the sample interfacial areas, which provided a fast and non-destructive means for acquiring bonding information of the materials. Figure 8 shows results of the Raman spectroscopy tests on the ABS. ABS has multiple Raman active modes from 1000 to 3200 cm^{-1} [see Figure 8(a)]. Tests were performed on both the surface of the printed build surfaces as well as bead–bead interfacial areas. The peaks displayed in the Raman spectra indicate the presence of acrylonitrile (A) due to C≡N stretch, butadiene (B) due to C═C stretch, and styrene (S) due to C—H aromatic bending.[19] Figure 8(b) shows the variations in the butadiene signal at 1667 cm *trans* and 1653 cm *cis* that were observed at various points in the maps due to different orientations of C═C bonding. Figure 8(c) shows Raman spectroscopy maps of the S2, S3, H2, and H3 samples. Each map is oriented with build-interface-build running from top to bottom. The relative amount of butadiene was determined by considering the ratio of the averaged B/S intensity for each location within the map. A baseline correction was made to each peak before calculating the ratios. For all scans, a similar pattern was observed for the B/A ratio. For all samples, the interfacial regions contained areas with B/S ratios only 65% of the response typically seen on the respective builds. Scans on H2, the sample with the longest rasters and thus shortest time for bead–bead interaction in the melt state, had a relatively uniform area of low butadiene content at the

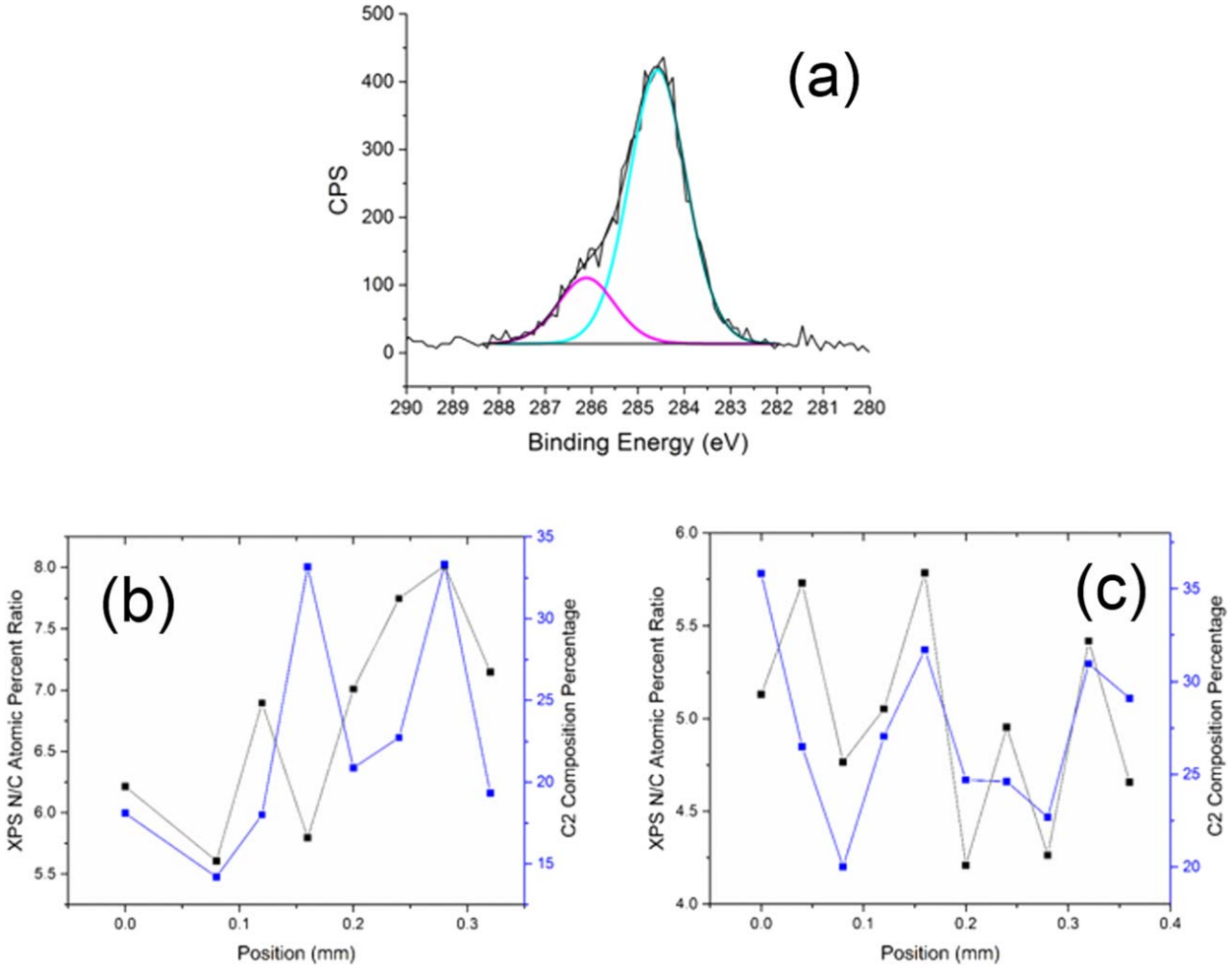

Figure 9. (a) Analysis of high-resolution C 1s XPS spectra of H2 surface. Figures (b) and (c) display N/C atomic ratios as well as acrylonitrile composition (C2) for H2 and S3 samples, respectively. [Color figure can be viewed in the online issue, which is available at wileyonlinelibrary.com.]

interface. Alternatively, the scans on S3, the sample with the shortest rasters and thus longest time for bead–bead interaction in the melt state, showed a more continuous B/S response across the interface, although regions of low butadiene content were still present. As noted previously, the rubbery B-phase of the feedstock material consists of variable-sized particles ranging from ~50 nm to 200 microns. Thus, depending on the time allowed for neighboring beads to interact in the melt state, less of the larger B-phase particles are expected to be present at the interface. Local mechanical tests within areas of low B/S or B/A ratio would be more likely to result in a relatively stiff response due to the lower presence of the rubbery phase, while tests within areas of higher B/S or B/A ratio would be more likely to result in a compliant indentation response and higher loss modulus. The Raman maps provide insight into the quasi-static and dynamic mechanical results, although it should be noted that the Raman signal is a near surface bonding response. Alternatively, the local mechanical tests are measuring a response at a minimum of 1 μm from the surface, and further influenced by material up to 10 times the indentation depth due to the long range stresses that develop under the probe.[23]

The surface chemistry of printed ABS was also examined using XPS, which probes the top 1 nm to 10 nm of the surface. Data were collected every 40 μm using equivalent sized apertures. The high-resolution C 1s spectra of the H2 surface are displayed in Figure 9(a). The spectra were fit with two main carbon components, consisting of the hydrocarbon (C1, 65% to 82%) and the carbon of the nitrile group (C2, 18% to 35%). The spectra for the S2 and S3 build surfaces were nearly identical. The data from processing high resolution C 1s spectra are displayed in Figure 9(b,c) for the H2 and S3 samples, respectively. The left axis of the figures denotes the nitrogen-to-carbon (N/C) atomic percent ratio, which describes the relative amount of nitrogen or acrylonitrile on the surface. The right axis denotes the relative composition of the C2 component. Generally, there is good tracking of the N/C ratio and the C2 composition. This is expected since both describe the acrylonitrile composition at the surface as it is the only nitrogen containing polymer in the build. Sinusoidal behavior is apparent in both charts with the relative surface composition of acrylonitrile changing every 100 μm to 200 μm (approximate width of the builds). While this suggests a variation in the composition between the builds and

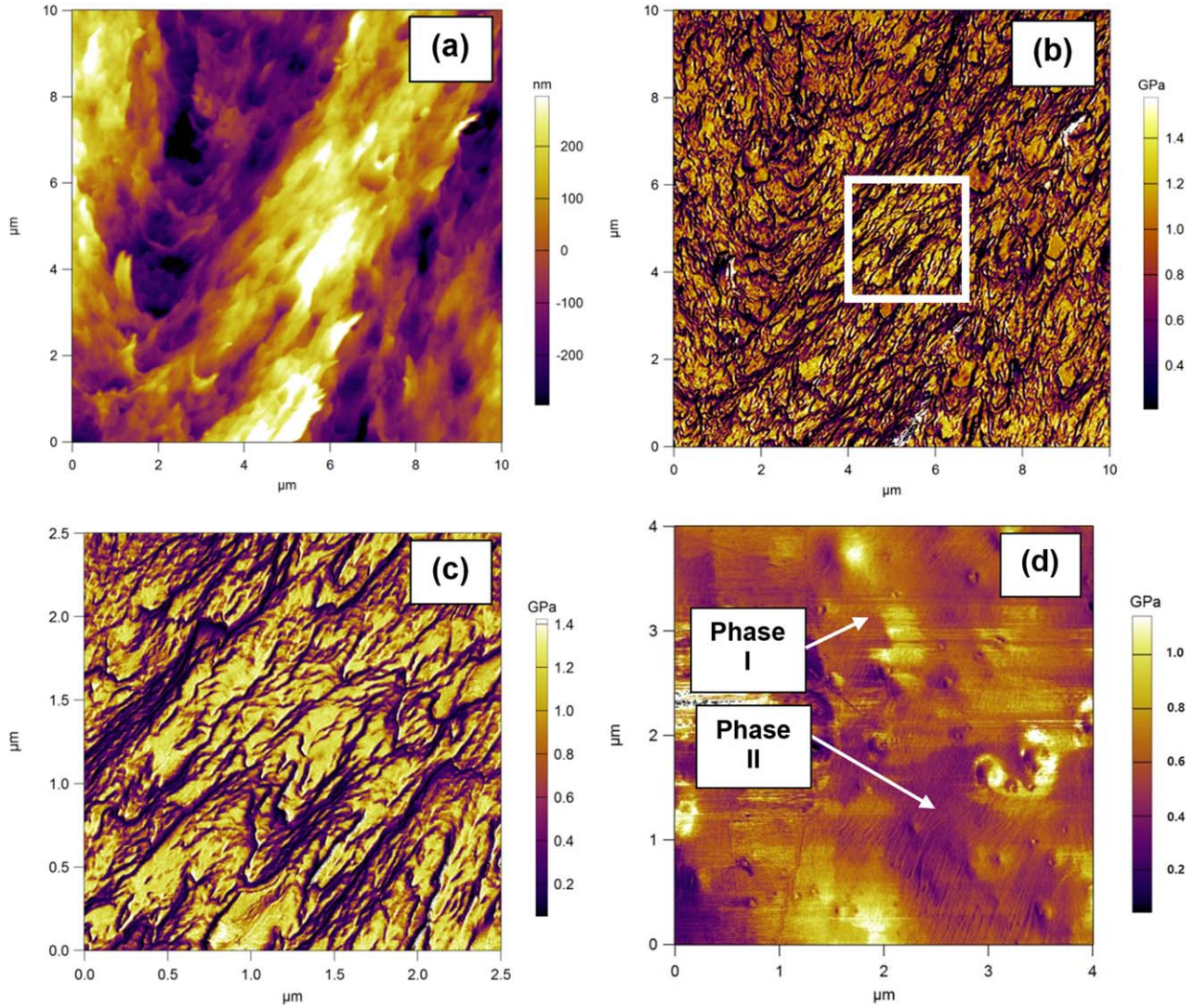

Figure 10. (a) 10 μm AFM height image of ABS tensile specimen fracture surface. (b) Corresponding elastic modulus map of region shown in (a). (c) 2.5 μm elastic modulus map of boxed region shown in (b). (d) 4 μm elastic modulus map of interfacial region. [Color figure can be viewed in the online issue, which is available at wileyonlinelibrary.com.]

interfaces, the lack of spatial resolution for the XPS tests limited the compositional information that could be extracted from the interfacial region.

AFM was used to characterize the morphology and near-surface mechanical properties of the printed specimens. Figure 10(a) includes an AFM height image inside a build fracture surface, while Figure 10(b) displays the corresponding elastic modulus map. Figure 10(c) displays a 2.5 μm zoom of the modulus map shown in Figure 10(b). The topography within the fractured build appears to show directional features running from bottom left to top right, while the elastic modulus maps show moderate variations which could be due to different phases. Figure 10(d) displays an elastic modulus map of the free surface of the interfacial region between builds. Multiple phases are more apparent on the free surface and give insight into the local mechanical behavior of the build–build interface.

Several considerations should be made when comparing the mechanical behavior of these materials across length scales. Many semicrystalline and amorphous polymers have been shown to possess a correlation between microscale hardness tests and bulk mechanical properties.[22] A model relating the yield stress to the elastic modulus was developed by considering the forces acting between two molecules.[41] These previous efforts resulted in the empirical prediction $H \approx E/10$, where the elastic modulus was measured through bulk tensile experiments. Supporting Information Figure S1 plots the H vs. E data for the bulk tensile tests and quasi-static indentation experiments with the corrections applied for the measured creep. The results from the various tests agree reasonably well with the empirical results reported by Flores *et al.* for a semicrystalline polymer,[22] although we caution that the material tested in this work is fundamentally different (an amorphous, heterogeneous

polymer consisting of a stiff matrix with relatively compliant inclusions).

For the nanoscale mechanical tests, the AFM modulus maps represent the local elastic response between the AFM probe and the first few nanometers of the sample. The AFM elastic modulus values found in this study are reasonably close to the results found through bulk mechanical testing and instrumented indentation. However, the AFM modulus results are typically lower than the elastic modulus values found through the other tests, which is likely due to fundamental differences in the mechanical characterization methods or bulk versus surface effects. AFM tests are carried out with a 10 nm tip, while nanoindentation measurements use a probe ~10 times larger. Thus, nanoindentation measures a larger extent of variability with respect to AFM (topographic variability, higher degree of defects, testing multiple phases, etc.), while bulk tensile tests measure global mechanical properties of the printed specimens. Next, typical nanoindentation tests are elastic–plastic while AFM tests are assumed purely elastic. In addition, the anisotropy of the materials would prompt fundamentally different mechanical behavior when comparing the global tensile testing to nanoindentation and AFM-indentation, which are both primarily compressive. Lastly, the time-dependent mechanical properties of the material were expected to result in a range of measured mechanical behavior depending on the testing rates (the global tensile tests are quasi-static, AFM modulus mapping is executed in kHz to MHz rates, and local DMA tests were performed in the 0.1–100 Hz range).

CONCLUSIONS

This research effort explored the mechanical behavior of acrylonitrile butadiene styrene specimens processed through FDM under several printed configurations. Bulk tensile tests were compared to local mechanical properties found through nanoindentation, local dynamic mechanical analysis, and atomic force microscopy modulus mapping. An interfacial stiffening effect was found for the majority of the specimens tested, with up to a 40% increase in the indentation elastic modulus found for the samples with relatively long rasters and thus less time for bead–bead interaction in the melt state. Raman spectroscopy mapping showed a lack of the rubbery butadiene phase at the interface, with 30–40% lower butadiene/styrene and butadiene/acrylonitrile ratios typically found, with respect to measurements on the build surfaces. The lack of the rubbery phase at these boundaries was expected to be responsible for the poor bulk mechanical behavior seen with several print configurations. The results provide insight into the multiscale mechanical behavior of ABS structures processed through FDM and offer a general roadmap for future mechanical testing on additive manufactured components.

ACKNOWLEDGMENTS

The authors thank Jonathan Seppala, Chelsea Davis, and Christopher White at the National Institute of Standards and Technology (NIST) for helpful insights into processing and characterization of ABS. The authors acknowledge Ray Von Wahlde and Steven Biggs for help with specimen processing, Johnny Thiravong and Travis Bogetti for help with tensile tests, and Christopher da Rosa for help with renderings.

REFERENCES

1. Boschetto, A.; Bottini, L. *Int. J. Adv. Manuf. Technol.* **2014**, *73*, 913.
2. Torrado, A. R.; Shemelya, C. M.; English, J. D.; Lin, Y.; Wicker, R. B.; Roberson, D. A. *Addit. Manuf.* **2015**, *6*, 16.
3. Zhu, Z.; Dhokia, V.; Newman, S. T.; Nassehi, A. *Int. J. Adv. Manuf. Technol.* **2014**, *74*, 1115.
4. Feng, Y.; Siegmund, T.; Habtour, E.; Riddick, J. *Int. J. Adv. Manuf. Technol.* **2015**, *75*, 140.
5. Espalin, E.; Muse, D. W.; MacDonald, E.; Wicker, R. B. *J. Adv. Manuf. Technol.* **2014**, *72*, 963.
6. Vaezi, M.; Sietz, H.; Yang, S. *Int. J. Adv. Manuf. Technol.* **2013**, *67*, 1721.
7. Korpela, J.; Kokkari, A.; Korhonen, H.; Malin, M.; Narhi, T.; Seppala, J. *J. Biomed. Mater. Res. B* **2013**, *101*, 610.
8. Ang, K. C.; Leong, K. F.; Chua, C. K. *Rapid Prototyping J.* **2006**, *12*, 100.
9. Makitie, A. A.; Korpela, J.; Elomaa, L.; Reivonen, M.; Kokkari, A.; Malin, M.; Korhonen, H.; Wang, X. H.; Salo, J.; Sihvo, E.; Salmi, M.; Partanen, J.; Paloheimo, K. S.; Tuomi, J.; Narhi, T.; Seppala, J. *Acta Oto-Laryngol.* **2013**, *133*, 412.
10. Kim, K.; Dean, D.; Wallace, J.; Breithaupt, R.; Mikos, A. G.; Fisher, J. P. *Biomaterials* **2011**, *32*, 3750.
11. Turner, B. N.; Strong, R.; Gold, S. A. *Rapid Prototyping J.* **2014**, *20*, 192.
12. Bellini, A.; Guceri, S.; Bertoldi, M. *J. Manuf. Sci. E-T ASME* **2004**, *126*, 237.
13. Rosenzweig, N.; Narkis, M. *Polym. Eng. Sci.* **1981**, *21*, 1167.
14. Bellehumeur, C.; Li, L.; Sun, Q.; Gu, P. *J. Manuf. Process* **2004**, *6*, 170.
15. Sun, Q.; Rizvi, G. M.; Bellehumeur, C. T.; Gu, P. *Rapid Prototyping J.* **2008**, *14*, 72.
16. Boronat, T.; Segui, V.; Peydro, M.; Reig, M. *J. Mater. Process. Technol.* **2009**, *209*, 2735.
17. Ahn, S.; Montero, M.; Odell, D.; Roundy, S.; Wright, P. K. *Rapid Prototyping J.* **2002**, *8*, 248.
18. Lugo, M.; Fountain, J. E.; Hughes, J. M.; Bouvard, J.; Horstemeyer, M. F. *J. Appl. Polym. Sci.* **2014**, *131*, DOI: 10.1002/app.40882.
19. Marissen, R.; Schudy, D.; Kemp, A. V. J. M.; Coolen, S. M. H.; Duijzings, W. G.; Van der Pol, A.; ; Van Gulick, A. J. *J. Mater. Sci.* **2001**, *36*, 4167.
20. Es-Said, O. S.; Foyos, J.; Noorani, R.; Mendelson, M.; Marloth, R.; Pregger, B. A. *Mater. Manuf. Process* **2000**, *15*, 107.
21. Sood, A. K.; Ohdar, R. K.; Mahapatra, S. S. *Mater. Des.* **2010**, *31*, 287.
22. Flores, A.; Calleja Balta, F. J.; Bassett, D. C. *Polymer* **2000**, *41*, 5431.

23. Oliver, W. C.; Pharr, G. M. *J. Mater. Res.* **1992**, *7*, 1564.
24. Saha, R.; Nix, W. D. *Acta Mater.* **2002**, *50*, 23.
25. Forster, A. M.; Michaels, C. A.; Sung, L.; Lucas, J. *ACS Appl. Mater. Interface* **2009**, *1*, 597.
26. Gershon, A.; Cole, D. P.; Kota, A. K.; Bruck, H. A. *J. Mater. Sci.* **2010**, *45*, 6353.
27. Cole, D. P.; Reddy, A. L. M.; Hahm, M. G.; McCotter, R.; Hart, A. H. C.; Vajtai, R.; Ajayan, P. M.; Karna, S. P.; Bundy, M. L. *Adv. Energy Mater.* **2014**, *4*, 1300844.
28. Soifer, Y. M.; Verdyan, A.; Kazakevich, M.; Rabkin, E. *Mater. Lett.* **2005**, *59*, 1434.
29. Jakes, J. E.; Frihart, C. R.; Beecher, J. F.; Moon, R. J.; Stone, D. S. *J. Mater. Res.* **2008**, *23*, 1113.
30. Cole, D. P.; Jin, H.; Lu, W.; Roytburd, A. L.; Bruck, H. A. *Appl. Phys. Lett.* **2009**, *94*, 193114.
31. Cole, D. P.; Bruck, H. A.; Roytburd, A. L. *J. Appl. Phys.* **2008**, *103*, 064315.
32. Cole, D. P.; Bruck, H. A.; Roytburd, A. L. *Strain* **2009**, *45*, 232.
33. Van Landingham, M. R.; Chang, N. K.; Drzal, P. L.; White, C. C.; Change, S. H. *J. Polym. Sci. Part B: Polm. Phys.* **2005**, *43*, 1794.
34. White, C. C.; Van Landingham, M. R.; Drzal, P. L.; Chang, N. K.; Chang, S. H. *J. Polym. Sci. Part B: Polm. Phys.* **2005**, *43*, 1812.
35. Giro-Paloma, J.; Roa, J. J.; Diez-Pascual, A. M.; Flores, A.; Martinez, M.; Chimenos, J. M.; Fernandez, A. I. *Eur. Polym. J.* **2013**, *49*, 4047.
36. Feng, G.; Ngan, A. H. W. *J. Mater. Res.* **2002**, *17*, 660.
37. Xu, Z.; Li, X. *Acta Mater.* **2006**, *54*, 1699.
38. Cole, D. P.; Strawhecker, K. E. *J. Mater. Res.* **2014**, *29*, 1104.
39. McAllister, Q.; Gillespie, J. W.; Van Landingham, M. R. *J. Mater. Res.* **2012**, *27*, 197.
40. McAllister, Q.; Gillespie, J. W.; Van Landingham, M. R. *J. Mater. Res.* **2012**, *27*, 1824.
41. Struik, L. C. E. *J. Non-Cryst. Solids* **1991**, *131–133*, 395.